frontiers | Frontiers in Earth Science

ORIGINAL RESEARCH
published: 01 July 2022
doi: 10.3389/feart.2022.887154

Metamorphic *P–T* Evolution and *In Situ* Biotite Rb–Sr Geochronology of Garnet–Staurolite Schist From the Ramba Gneiss Dome in the Northern Himalaya

Long-Long Gou[1], Xiao-Ping Long[1]*, Hao-Yu Yan[1], Tian-Chu Shu[2], Jing-Yu Wang[1], Xiao-Fei Xu[1], Feng Zhou[1] and Zhi-Bo Tian[1]

[1]State Key Laboratory of Continental Dynamics, Department of Geology, Northwest University, Xi'an, China, [2]Department of Earth and Environmental Sciences, RC Centre of Excellence for Core to Crust Fluid Systems, Macquarie University, Sydney, NSW, Australia

OPEN ACCESS

Edited by:
Yi Chen,
Institute of Geology and Geophysics (CAS), China

Reviewed by:
Hao Wang,
Institute of Geology and Geophysics (CAS), China
Jia-Min Wang,
Institute of Geology and Geophysics (CAS), China

****Correspondence:***
Xiao-Ping Long
longxp@nwu.edu.cn

Specialty section:
This article was submitted to Petrology, a section of the journal Frontiers in Earth Science

Received: *01 March 2022*
Accepted: *23 May 2022*
Published: *01 July 2022*

Citation:
Gou L-L, Long X-P, Yan H-Y, Shu T-C, Wang J-Y, Xu X-F, Zhou F and Tian Z-B (2022) Metamorphic P–T Evolution and In Situ Biotite Rb–Sr Geochronology of Garnet–Staurolite Schist From the Ramba Gneiss Dome in the Northern Himalaya. Front. Earth Sci. 10:887154. doi: 10.3389/feart.2022.887154

The North Himalayan gneiss domes provide a window for looking into the deeper crust and record abundant clues of continent collisional orogenesis. This study carried out detailed petrology, *in situ* LA–ICP–MS biotite Rb–Sr dating, and phase equilibrium modeling on garnet–staurolite–two-mica schist in the Ramba gneiss dome in order to constrain metamorphic *P–T* evolution and the timing of metamorphism. A clock-wise *P–T* path, involving an early prograde process that evolves from ~540°C at ~4.4 kbar to ~630°C at ~6.0 kbar, was constructed for garnet–staurolite–two-mica schist in the Ramba gneiss dome. *In situ* LA–ICP–MS biotite Rb–Sr analysis yielded two metamorphic ages of 37.17 ± 5.66 and 5.27 ± 3.10 Ma, corresponding to the timing of retrograde cooling and the cooling age of the dome following the thermal resetting by the emplacement of ca. 8 Ma leucogranite pluton in the core of the dome, respectively. The peak metamorphism is inferred to be older than ca. 37 Ma. Based on these results and the data previously published, the garnet–staurolite–two-mica schist recorded the Eocene crustal thickening, following the India–Asia collision and later the exhumation process.

Keywords: phase equilibrium modeling, P–T path, Ramba gneiss dome, E–W extension, northern Himalaya

INTRODUCTION

Gneiss domes are ubiquitous structures in exhumed orogens (Whitney et al., 2004). During orogenesis, gneiss domes vertically transfer large volumes of deep-seated material into the upper crustal level (Teyssier and Whitney, 2002; Rey et al., 2017) and, thus, provide a window to investigate the orogenic process in the middle-to-lower crust. In addition, gneiss domes are often formed by the superposition of several dome-forming mechanisms or in several different tectonic settings (Yin, 2004). Therefore, gneiss domes were used to investigate the fundamental orogenic process and geodynamics of continental collision orogen, such as crustal thickening or shortening (Yin, 2006; Smit et al., 2014; Ding et al., 2016a) and extension (Lister and Davis, 1989; Chen et al., 1990; Lee and Whitehouse, 2007; Wang et al., 2018).

The Himalayan orogen, as the result of the ongoing collision between the Indian and Asian plates, is one of the largest collisional orogens on the Earth (**Figure 1**), which played a central role in

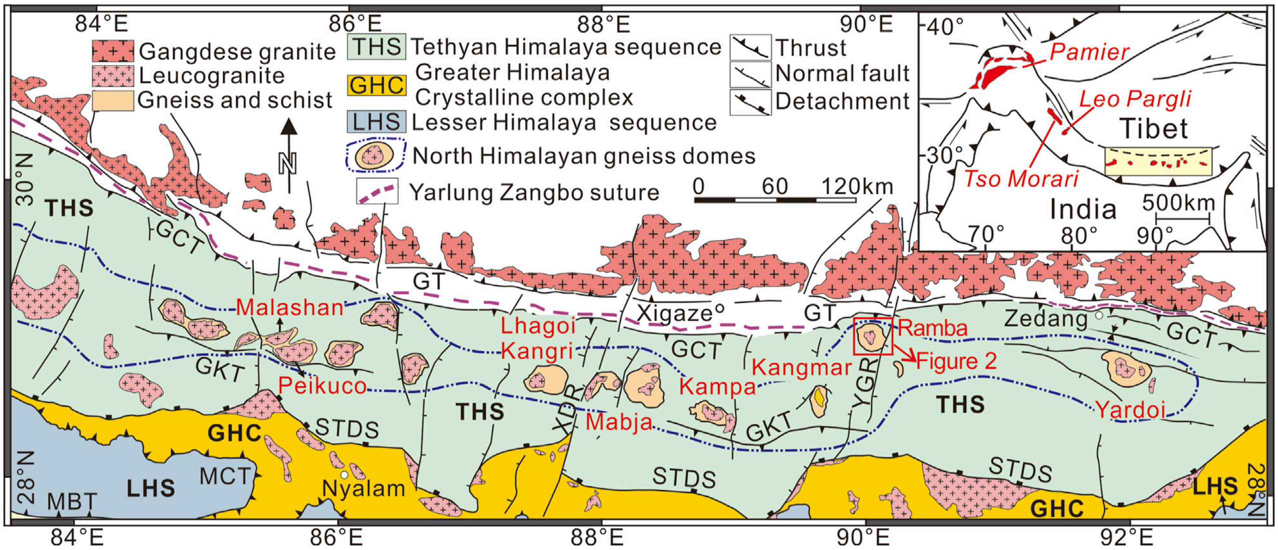

FIGURE 1 | Generalized geological map of the Himalayan orogen (modified from Wang et al., 2018). Abbreviations of metamorphic complexes: GT, Gangdese thrust; GCT, Greater Counter thrust; GKT, Gyirong–Kangmar thrust; STDS, south Tibetan detachment system; MCT, main central thrust; MBT, main boundary thrust.

understanding the continent–continent collisional orogenesis (Yin and Harrison, 2000; Beaumont et al., 2001; Harris, 2007; Searle et al., 2009; Palin et al., 2014; Wang et al., 2016). The northern Himalayan belt is characterized by extension structures, including the north Himalayan gneiss domes (NHGDs), the south Tibet detachment system (STDS), and the north–south trending rifts (NSTR) (Zhang et al., 2012). During the past few decades, the formation mechanisms of the NHGD have been the subject of intensive studies (Chen et al., 1990; Lee et al., 2000, 2004, 2006; Aoya et al., 2006; Quigley et al., 2008; Stearns et al., 2013; Zhang et al., 2004, 2012; Ding et al., 2016a, b; Jessup et al., 2019) as the NHGDs are the window to the middle-to-lower crust in the northern Himalayan belt and are the key to understand not only the tectonic evolution of the Himalayan orogen but also the geodynamic processes within the middle-to-lower crust of continent–continent collisional orogens. Different geodynamic settings have been proposed to interpret the formation of the NHGD, such as north–south extension with the top-to-north movement along the STDS (Chen et al., 1990; Lee et al., 2000, 2004, 2006; Wang et al., 2018), diapirism of buoyant anatexis (LeFort et al., 1987; Harrison et al., 1997), and east–west extension related to the NSTR (Zhang and Guo, 2007; Zhang et al., 2012; Fu et al., 2016).

The Ramba gneiss dome, which is dominated by the top-to-E shear structure, was considered to have been formed by the E–W extension along the NSTR (Guo et al., 2008; Zhang et al., 2012). However, due to the lack of metamorphic data for the Ramba gneiss dome up to now, the similarities and differences of the metamorphic P–T–t evolution between the Ramba gneiss dome and other famous gneiss domes (the Mabja dome and the Yardoi gneiss dome) are unclear.

In this article, the metamorphic P–T evolution and the timing of metamorphism for garnet–staurolite–two-mica schist in the Ramba gneiss dome were constrained, with the evidence from detailed petrology, *in situ* LA–ICP–MS biotite Rb–Sr dating, and phase equilibrium modeling. Based on these results, the tectonic implications and the differences in metamorphic evolution between the E–W and the N–S extensional North Himalayan gneiss domes were discussed.

GEOLOGICAL SETTING AND SAMPLES

The Himalayan orogen includes the northern Himalayas and the southern Himalayas, which are separated by the high crest line (Yin, 2006). The STDS is a network of detachment faults, juxtaposing the Tethys Himalayan sequences (THSs) in the hanging wall over the Greater Himalayan Crystallines (GHC) in the footwall (Searle and Godin, 2003; Zhang et al., 2012). The southern Himalayas is composed of the GHC, the Lesser Himalayan sequences (LHSs), and the Siwalik group (Zhang et al., 2012; **Figure 1**). The GHC is characterized by the ca. 40–30 Ma high pressure (HP) granulite-facies rocks (Kohn and Corrie, 2011; Regis et al., 2014; Iaccarino et al., 2015; Zhang et al., 2015), the ca. 17–14 Ma granulitized eclogites (Wang Y. et al., 2017, 2021; Li et al., 2019; Zhang et al., 2021; Wu et al., 2022), Barrovian metamorphic belts (Wang et al., 2013, 2015; Iaccarino et al., 2017; Shrestha et al., 2017), and abundant ca. 33–7 Ma leucogranites (Searle et al., 1999; Searle and Godin, 2003; Wu et al., 2015 and references therein; Gou et al., 2016; Hopkinson et al., 2017; Liu et al., 2022a). It underwent a long-lived partial melting from ca. 40 to 8 Ma (e.g., Wang et al., 2013, 2015, Wang et al., 2017 J.-M.; Zhang et al., 2015; Tian et al., 2019; Liu et al., 2022b). Within the GHC, tectono-metamorphic discontinuities have been recognized in the recent decade (Wang et al., 2016, and references therein).

The northern Himalayan belt is dominated by the THS, consisting of unmetamorphosed to low-grade metasedimentary rocks (Zhang et al., 2012; **Figure 1**). This belt is characterized by

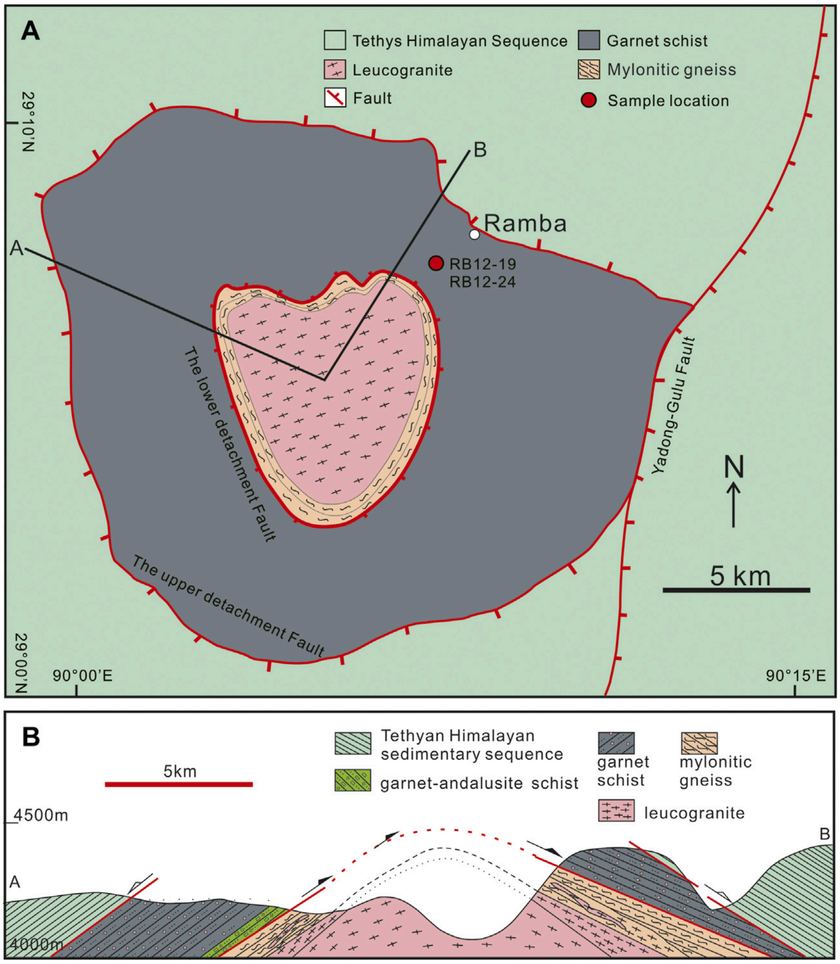

FIGURE 2 | (A) Schematic geological map showing the Ramba gneiss dome and **(B)** cross-section (modified from Zhang et al., 2012).

the NHGD cored by granite plutons (Zhang et al., 2012) and the crystallization ages of granites or leucogranites in the northern Himalayan belt ranging from ca. 48 to 8 Ma (Aikman et al., 2008; Zhang et al., 2012; Liu et al., 2014; Zeng et al., 2011; Gao et al., 2012; Wu et al., 2015; Zeng and Gao, 2017 and references). The dome geometry at the Mabja gneiss dome was formed by middle-Miocene southward-directed thrust faulting upward and southward, which are similar to those of the Kangmar dome (Lee et al., 2000, 2004, 2006). The peak metamorphic condition of the migmatite sample from the sillimanite-zone in the Mabja gneiss dome is 8.2 kbar/705°C (Lee et al., 2004), and the timing of peak metamorphism was constrained to be 35.0 ± 0.8 Ma (Lee and Whitehouse, 2007). The structural, metamorphic, and intrusive histories in middle crustal rocks exposed in these NHGD are similar to those in the GHC, suggesting that the middle crust was continuous from beneath the northern Himalayas southward to the high Himalayas (Lee et al., 2006; Lee and Whitehouse, 2007). The garnet–kyanite–staurolite schists of the Yardoi gneiss dome in the eastern Himalaya record peak $P–T$ conditions of 7–8 kbar and 630–660°C. Zircon U–Pb dating yielded metamorphic ages of 44.8 ± 1.1 Ma, 46.7 ± 1.8 Ma, and 48.2 ± 2.0 Ma (Ding et al., 2016a), which were considered as the timing of prograde metamorphism (Ding et al., 2016b), and Wang et al. (2018) obtained metamorphic ages of 18–17 Ma using SHRIMP monazite U/Th-Pb analysis and suggested that north–south extension in a convergent geodynamic setting during Early Miocene accounts for the formation of the Yardoi dome.

The Ramba gneiss dome is located on the west of the north–south trending Yadong–Gulu rift and near the Yarlung–Zanbo suture (Zhang et al., 2012; Liu et al., 2014, 2019; **Figures 1**, **2**). The dominant deformation was attributed to the E–W extension of the NSTR (Guo et al., 2008; Zhang et al., 2012). Liu et al. (2014) revealed that there were three epidotes (ca. 44 Ma, ca. 28 Ma, and ca. 8 Ma) of granitic magmatism. The granitic rocks of ca. 44 Ma and ca. 28 Ma occur as strongly deformed porphyritic two-mica granite gneiss dykes, which intruded into the margin of the dome (Liu et al., 2014, 2019). The ca. 8 Ma leucogranites include two-mica granite occupying the core of the dome and garnet-bearing granite dykes in the margin of the dome (Liu et al., 2014), and the former has biotite and muscovite $^{40}Ar/^{39}Ar$ ages of ca. 6 Ma (Guo et al., 2008).

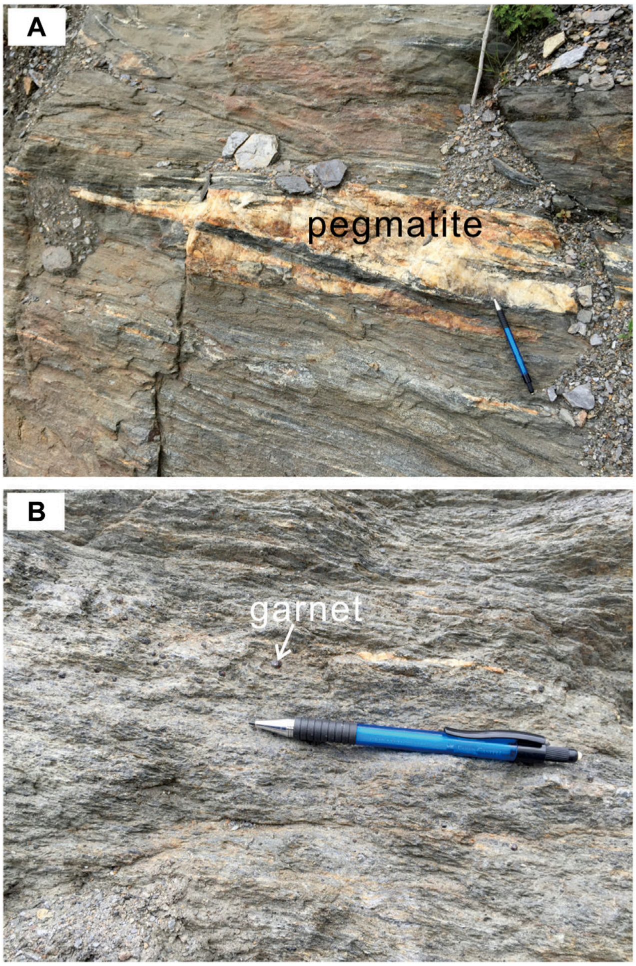

FIGURE 3 | Field photographs of garnet–staurolite–two-mica schist in the Ramba gneiss dome.

Here, two representative samples (RB12-19 and RB12-24) selected for this study are garnet–staurolite–two-mica schist, belonging to the base of the THS on the basis of rock association in a previous study, which experienced detachment shear of STDS (Guo et al., 2008; Zhang et al., 2012). These samples display porphyroblastic texture and are in gray color (**Figure 3**). Pegmatites that are parallel to foliation can be observed (**Figure 3A**), and garnet porphyroblasts are obvious on the outcrop (**Figure 3B**).

PETROGRAPHY AND MINERAL CHEMISTRY

Mineral compositions were analyzed using the JEOL JXA-8230 electron microprobe at the State Key Laboratory of Continental Dynamics (SKLCD), Northwest University, Xi'an. The operating conditions were 2 μm beam size, 15 kV acceleration voltage, and 10 nA beam current. Mineral abbreviations in this study follow Whitney and Evans (2010). Compositional maps illustrating the distributions of Fe, Mg, Ca, and Mn were obtained for representative garnet porphyroblasts using the Quanta450 FEG field-emission environmental scanning electron microscope coupled with the X-MaxN 50 X-ray energy dispersive spectrometer at the SKLCD.

Sample RB12-19

This sample consists of garnet (10%), staurolite (20%), biotite (25%), muscovite (10%), plagioclase (5%), and quartz (30%) and accessory minerals, including zircon, graphite, and ilmenite (**Figures 4A, B**). Garnet occurs as euhedral to subhedral porphyroblasts with grain sizes of 0.4–1.1 mm in diameter (**Figures 4A, B**), with minor quartz inclusions. Staurolite is present as a subhedral porphyroblast with grain sizes of 0.4–1.0 mm and is generally in contact with garnet (**Figures 4A, B**); it displays a yellow-to-black color due to abundant graphite inclusion. Biotite and muscovite occur in the matrix and define the foliation (**Figure 4A**). Plagioclase occurs as relatively small crystals in the matrix, and quartz occurs as small grains in the matrix or as mineral inclusions in garnet (**Figures 4A–C**). As a result, the peak metamorphic mineral assemblage is inferred to be garnet–biotite–muscovite–plagioclase–staurolite–ilmenite–quartz–H_2O.

Mineral compositions and the mole fractions of end-members for sample RB12-19 are given in **Supplementary Table S1**. The garnet is almandine-rich (X_{Alm} = 0.72–0.83), with low concentrations of spessartine (X_{Sps} = 0.07–0.18), pyrope (X_{Prp} = 0.04–0.09), and grossular (X_{Grs} = 0.04–0.06). The zoning profile of a representative garnet grain shows obvious compositional variation from core to rim (**Figure 5A**), with increasing almandine and decreasing spessartine but relatively flat pyrope and grossular, which are consistent with distributions of Fe, Mg, Ca, and Mn on garnet compositional maps (**Figure 6A**). Staurolite has homogeneous compositions, with X_{Mg} of 0.08–0.10. Biotite and muscovite also exhibit homogeneous compositions, with X_{Mg} of 0.40–0.41, Ti of 0.10–0.12 cations per formula unit (cpfu), and Si of 3.09–3.13 cpfu, respectively. Plagioclase displays no compositional variation between different grains, with X_{An} of 0.27–0.31.

Sample RB12-24

Sample RB12-24 is composed of garnet (10%), staurolite (10%), biotite (20%), muscovite (5%), plagioclase (20%), and quartz (35%) and accessory minerals, including zircon, graphite, and ilmenite (**Figures 4C,D**). Garnet occurs as subhedral porphyroblasts with grain sizes ranging from 0.5 to 2.7 mm (**Figure 4D**), larger than garnet in sample RB12-19 (**Figures 4A,B**); it contains mineral inclusions of quartz (**Figure 4D**). Staurolite is present as subhedral porphyroblasts with grain sizes of 0.3–1.4 mm and displays yellow-to-black color due to abundant graphite inclusion (**Figures 4C,E**). Both garnet and staurolite are wrapped by a continuous foliation delineated by biotite and muscovite in the matrix (**Figures 4D,E**). Plagioclase occurs as small grains in the matrix, and quartz occurs as small grains in the matrix or as mineral inclusions in garnet (**Figures 4D,E**). Therefore, the peak metamorphic mineral assemblage is inferred to be garnet–biotite–muscovite–plagioclase–staurolite–ilmenite–quartz–H_2O.

Mineral compositions and the mole fractions of end-members for sample RB12-24 are given in **Supplementary Table S2**. The

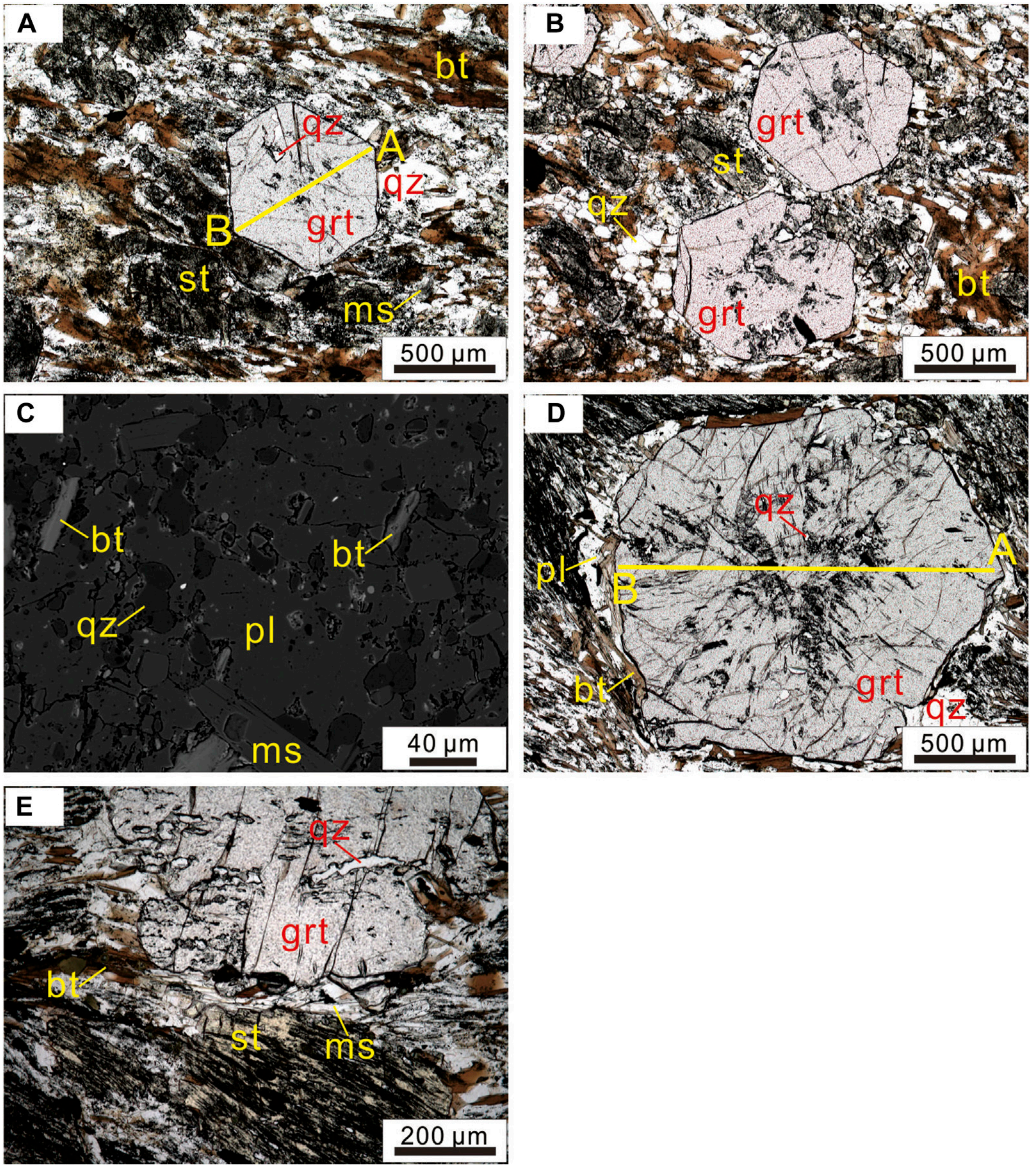

FIGURE 4 | Mineral assemblages and microstructures of garnet–staurolite–two-mica schist in the Ramba gneiss dome. **(A,B)** Photomicrographs to show garnet and staurolite porphyroblasts and matrix minerals, including biotite, muscovite, plagioclase, and quartz in sample RB12-19 (plane-polarized light). **(C)** Photomicrograph to show biotite, muscovite, quartz, and plagioclase in sample RB12-19 (back-scattered electron image). **(D)** Photomicrograph to show garnet porphyroblasts and matrix minerals, including biotite, muscovite, plagioclase, and quartz in the sample RB12-24 (plane-polarized light). **(E)** Photomicrographs to show garnet and staurolite porphyroblasts and matrix minerals, including biotite, muscovite, plagioclase, and quartz in sample RB12-24 (plane-polarized light).

garnet is almandine-rich (X_{Alm} = 0.75–0.87), with low pyrope (X_{Prp} = 0.03–0.04), spessartine (X_{Sps} = 0.01–0.08), and grossular (X_{Grs} = 0.09–0.14) (**Figure 5B**). Compared to those of the sample RB12-19, the pyrope is lower, whereas the grossular is higher (**Figures 5A,B**). The compositional profile of a representative garnet porphyroblast shows moderate variation from the core to the rim (**Figure 5B**), involving increasing almandine and decreasing spessartine but flat pyrope and grossular. These are consistent with distributions of Fe, Mg, Ca, and Mn on garnet compositional maps (**Figure 6B**). Staurolite is uniform in composition, with X_{Mg} ranging from 0.07 to 0.08. Biotite and muscovite also have homogeneous compositions, with X_{Mg} of 0.33–0.35, Ti of 0.10–0.12 cpfu, and Si of 3.08–3.12 cpfu, respectively. Plagioclase displays moderate compositional variation between different grains and is more calcic than that in sample RB12-19, with X_{An} of 0.38–0.53.

PHASE EQUILIBRIUM MODELING

The bulk chemical compositions (**Table 1**) were determined by wavelength-dispersive X-ray fluorescence (XRF) spectrometry on

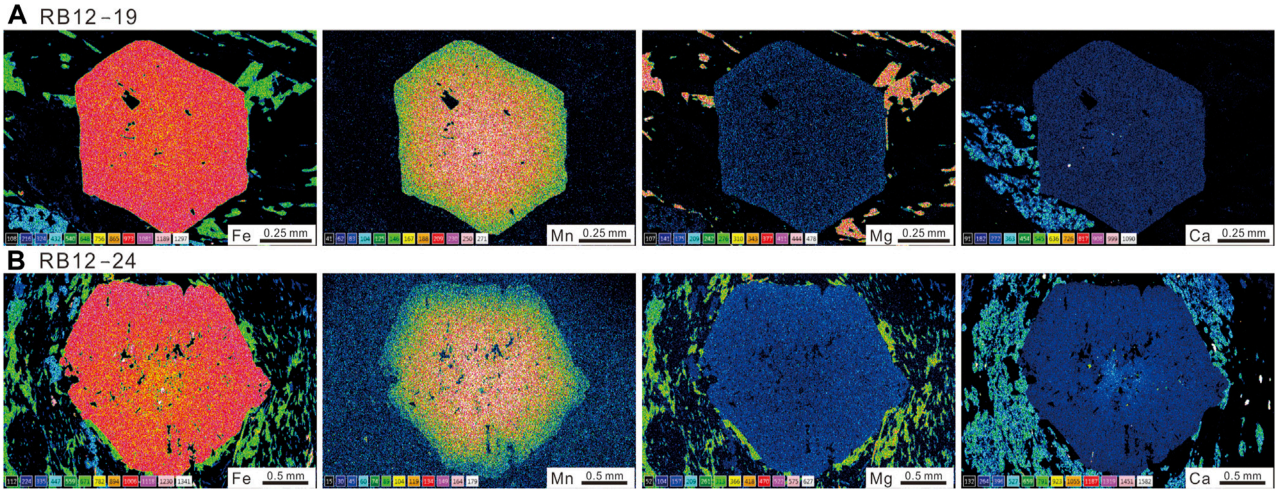

FIGURE 5 | Compositional mapping images of garnets in schist samples RB12-19 **(A)** and RB12-24 **(B)**.

a fused bead at the SKLCD, Northwest University, Xi'an. The normalized molar proportions used for the phase equilibrium modeling are given in **Table 1**. H_2O was set to be in excess. On the basis of low whole-rock Fe^{3+} contents as revealed that garnet, staurolite, biotite, and muscovite in two samples are low in Fe^{3+} (**Supplementary Tables S1, S2**), O = 0.010 was selected. The calculated *P*–*T* pseudosection allows the mineral assemblages to be evaluated within *P*–*T* conditions between 450 and 750°C and 3–9 kbar (**Figures 7, 8**). Phase equilibrium calculations were performed using Thermocalc version tc340 (Powell et al., 1998; updated October 2013) in the MnO–Na_2O–CaO–K_2O–FeO–MgO–Al_2O_3–SiO_2–H_2O–TiO_2–O_2 (MNCKFMASHTO) system, with the internally consistent thermodynamic dataset ds62 (Holland and Powell, 2011). The activity–composition (*a*–*x*) models for garnet, staurolite, biotite, cordierite, and chlorite are from White et al. (2014a, b), plagioclase from Holland and Powell (2003), ilmenite from White et al. (2000), epidote from Holland and Powell (2011), and muscovite and paragonite from Smye et al. (2010). Pure phases included sillimanite, kyanite, andalusite, quartz, and rutile. The mineral abbreviations in this study follow those by Whitney and Evans (2010).

Sample RB12-19

The peak phase assemblage is represented by the quinivariant field grt–bt–ms–pl–st–ilm–qz–H_2O, which has a wide *P*–*T* range, with upper pressure and temperature of 670°C and 7 kbar, respectively (**Figure 7A**). The chlorite-in and plagioclase-out assemblage field boundaries mark the low-temperature limit of this field. The upper temperature and pressure limits are the sillimanite-in and rutile-in assemblage field boundaries, respectively.

Figure 7B shows calculated isopleths of X_{Sps} and X_{Grs} for garnet, X_{Mg} for staurolite, and X_{Ti} for biotite. In the peak phase assemblage field of grt–bt–ms–pl–st–ilm–qz–H_2O, the X_{Sps} in garnet decreases significantly as pressure increases, and X_{Ti} in biotite increases as temperature increases. Isopleths of $X_{Ti(Bt)}$ of 0.10–0.12 are consistent with Ti contents of biotite (**Supplementary Table S1**). The plotted isopleths of X_{Grs} for garnet are close to vertical and decrease as temperature increases. The X_{Mg} in staurolite ranges from 0.08 to 0.10 (**Supplementary Table S1**), with corresponding isopleths plotted in the phase assemblage fields of grt–ms–chl–pl–st–ilm–qz–H_2O and grt–bt–ms–chl–pl–st–ilm–qz–H_2O. As no prograde and retrograde metamorphic mineral assemblages were observed, isopleths of X_{Sps} and X_{Grs} for garnet, X_{Mg} for staurolite, and X_{Ti} for biotite were used to constrain the *P*–*T* evolution. Plagioclase is stable in the studied sample, and thus, mineral assemblages during the early prograde metamorphic stage should contain plagioclase. Therefore, the X_{Mg} isopleths of staurolite in the mineral assemblage fields that contain plagioclase can be used to constrain the *P*–*T* conditions in the early stage of prograde metamorphism, although the defined *P*–*T* range is relatively large (**Figure 7B**). X_{Sps} and X_{Grs} in garnet and X_{Ti} in biotite constrain the peak metamorphic *P*–*T* conditions to be ~630°C at ~5.8 kbar in the peak mineral assemblage field of grt–bt–ms–pl–st–ilm–qz–H_2O. As a result, a prograde *P*–*T* path that evolves roughly from ~540°C at ~4 kbar to ~630°C at ~5.8 kbar was defined for the sample RB12-19 (**Figure 7B**).

Sample RB12-24

The peak phase assemblage of grt–bt–ms–pl–st–ilm–qz–H_2O is represented by a quinivariant field, which occurs between 552 and 668°C and 4.7–6.9 kbar (**Figure 8A**). The sillimanite-in assemblage field boundary marks the upper-temperature limit of this field, and the rutile-in assemblage field boundary is the upper-pressure limit. The low temperature and pressure limits are the chlorite-in and muscovite-out assemblage field boundaries, respectively.

Figure 8B shows calculated isopleths of X_{Sps} and X_{Grs} for garnet and X_{Ti} for biotite. The isopleths of X_{Sps} in garnet are horizontal and decrease as pressure increases, and the isopleths of X_{Ti} in biotite are vertical and increase as temperature increases, in the peak phase assemblage field (grt–bt–ms–pl–st–ilm–qz–H_2O).

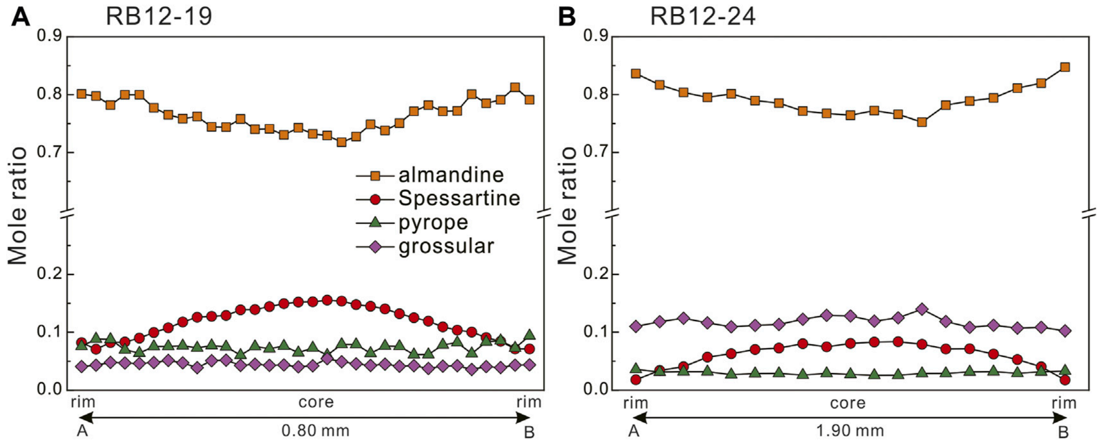

FIGURE 6 | Compositional profiles of garnet porphyroblasts from garnet–staurolite–two-mica schist samples RB12-19 **(A)** and RB12-24 **(B)**. **(A,B)** show garnet compositions matching those at the corresponding locations along the compositional profile of garnet in **Figure 4**.

Ti contents of biotite correspond to isopleths of $X_{Ti(Bt)}$ of 0.10–0.12 (**Supplementary Table S2**). In the phase assemblage field of grt–bt–ms–pl–chl–ilm–qz–H_2O, the isopleths of X_{Sps} in garnet are close to horizontal and decrease as temperature increases. The plotted isopleths of X_{Grs} for garnet are near vertical and decrease as temperature increases. Similar to sample RB12-19, isopleths of X_{Sps} and X_{Grs} for garnet and X_{Ti} for biotite were used to constrain the P–T evolution. The X_{Sps} and X_{Grs} in the garnet core and mantle have crossover points in the mineral assemblage field grt–bt–ms–chl–pl–ilm–qz–H_2O, which constrain the P–T conditions in the early stage of prograde metamorphism to be ~540°C at ~4.4 kbar (**Figure 8B**). In addition, the crossover points of X_{Sps} and X_{Grs} in the garnet rim fall into the peak phase assemblage field of grt–bt–ms–pl–st–ilm–qz–H_2O, which is close to or within the P–T range defined by isopleths of X_{Ti} for biotite (**Figure 8B**). As a result, a prograde P–T path that evolves from ~540°C at ~4.4 kbar to ~620°C at ~6.3 kbar was acquired for the sample RB12-24 (**Figure 8B**).

LA–ICP–MS BIOTITE RB–SR GEOCHRONOLOGY

In situ biotite Rb–Sr dating was conducted on garnet–staurolite–two-mica schist samples RB12-19 and RB12-24. Biotite Rb–Sr isotopic compositions were analyzed on thin sections (**Figure 9**) using an NWR 193-nm ArF excimer laser-ablation (LA) system coupled to an inductively coupled plasma mass spectrometry (ICP-MS, iCAP TQ 00108) at the Guangzhou Tuoyan Analytical Technology Co., Ltd., Guangzhou, China. Ablation material was carried out with high-purity He gas, which was then mixed with Ar gas before introduction into the ICP-MS torch. The reaction gas N_2O was used to suppress isobaric interferences as N_2O is a highly potent reaction gas that reacts efficiently with Sr^+ to form SrO^+ ions but not with Rb^+ (Hogmalm et al., 2017). The reaction rates are optimized by increasing N_2O flow rates in the reaction cell and monitoring the sensitivity of Sr^+ and SrO^+ whilst ablating NIST SRM 610 and mica-Mg. It was found that the signals of SrO^+ achieve maximum without significant loss in the Rb^+ signal when using N_2O at 25–27% flow rates (0.25–0.27 ml min^{-1} of N_2O).

Before sample measurements, N_2O was connected to the 4th mass flow controller in the iCAP TQ, and the lines were purged at a 25% flow rate (0.25 ml min^{-1} of N_2O) for 2 h to maintain stability. This procedure washes out gas impurities and saturates the system, minimizing drift due to variations in the reaction rate. Then, the lens and cell parameters were tuned to maximize sensitivity by ablating NIST SRM 610 in the line scan mode (spot size, 30 μm; pulse repetition rate, 10 Hz; fluence, ~3.5 J/cm^2). Each analysis consists of 30 s of background acquisition followed by 120 s of ablation and 30 s of washout. A dwell time of 50 ms was used for the analysis of on-mass and mass-shifted Sr isotopes (^{86}Sr, ^{87}Sr and ^{88}Sr, ^{86}Sr^{16}O, ^{87}Sr^{16}O, and ^{88}Sr^{16}O) and ^{85}Rb. Typical laser settings during sample analysis are 110-μm spot size, ~7 J/cm^2, and 5-Hz pulse repetition. The detailed instrumentation and analytical conditions were set, following the method described by Gorojovsky and Alard (2020). The raw data were exported offline, and the whole data reduction procedure was performed using an Excel macro program. The Mica-Mg was used as a primary reference standard for calibration of isotopic ratios of the samples. The standard NIST SRM 610 was used as secondary reference material to monitor the data quality, and the measured ^{87}Rb/^{86}Sr and ^{87}Sr/^{86}Sr ratios are 2.16 ± 0.08 (n = 2, 2σ) and 0.7110 ± 0.0048 (n = 2, 2σ), respectively. Compared with the recommended ratios for the standard NIST SRM 610 (^{87}Rb/^{86}Sr = 2.33, Gorojovsky and Alard, 2020; ^{87}Sr/^{86}Sr = 0.709699 ± 0.000018, Woodhead and Hergt, 2001), the measured ^{87}Sr/^{86}Sr ratio is similar within error, whereas the measured ^{87}Rb/^{86}Sr ratio is slightly lower, which may be due to that the external standard Mica-Mg has a high ^{87}Rb/^{86}Sr ratio (154–155, Gorojovsky and Alard, 2020).

TABLE 1 | Bulk compositions used for phase equilibrium modeling.

Whole-rock compositions (wt.%)												
Sample	SiO2	TiO_2	Al_2O_3	Fe_2O_3	MnO	MgO	CaO	Na_2O	K_2O	P_2O_5	LOI	Total
RB12-19	59.37	0.82	20.56	10.10	0.28	1.87	0.50	0.54	3.12	0.11	2.60	99.87
RB12-24	55.45	0.95	21.09	9.47	0.11	1.57	4.31	2.03	1.98	0.13	2.59	99.68

Normalized molar proportion used for phase equilibrium modeling												
Sample	Figures	H2O	SiO_2	Al_2O_3	CaO	MgO	FeO	K_2O	Na_2O	TiO_2	MnO	O
RB12-19	7	excess	69.209	14.123	0.624	3.250	8.859	2.320	0.610	0.719	0.276	0.010
RB12-24	8	excess	64.471	14.449	5.369	2.721	8.285	1.468	2.288	0.831	0.108	0.010

Notes: LOI, loss on ignition.

Sample RB12-19

A total of 19 spot analyses were carried out on biotite in sample RB12-19. During a single spot analysis, spots 1, 6, and 7 yielded multiple intervals with obviously different ratios of $^{87}Rb/^{86}Sr$ and $^{87}Sr/^{86}Sr$, which imply biotite may have inhomogeneous Rb–Sr isotopic compositions. Thus, these spot analyses obtained more than one effective data (**Table 2**). The Rb–Sr isotopic data of 3, 6.2, 7.2, 8, 14, 16, 17, and 18 were excluded during age calculation as these data are scattered on the $^{87}Rb/^{86}Sr$ and $^{87}Sr/^{86}Sr$ isochron diagram and cannot be well-included into an isochron (**Figure 9A**). The remaining $^{87}Rb/^{86}Sr$ and $^{87}Sr/^{86}Sr$ ratios are 3.7942–131.847 and 0.7062–0.7866, respectively, which yielded an isochron age of 37.17 ± 5.66 Ma (n = 16, MSWD = 1.5).

Sample RB12-24

Similar to sample RB12-19, 19 spot analyses were carried out on biotite in sample RB12-24. Spot 17 yielded multiple intervals with obviously different ratios of $^{87}Rb/^{86}Sr$ and $^{87}Sr/^{86}Sr$, which obtained two effective datasets (**Table 2**). The $^{87}Rb/^{86}Sr$ and $^{87}Sr/^{86}Sr$ ratios of biotite in sample RB12-24 range from 0.763

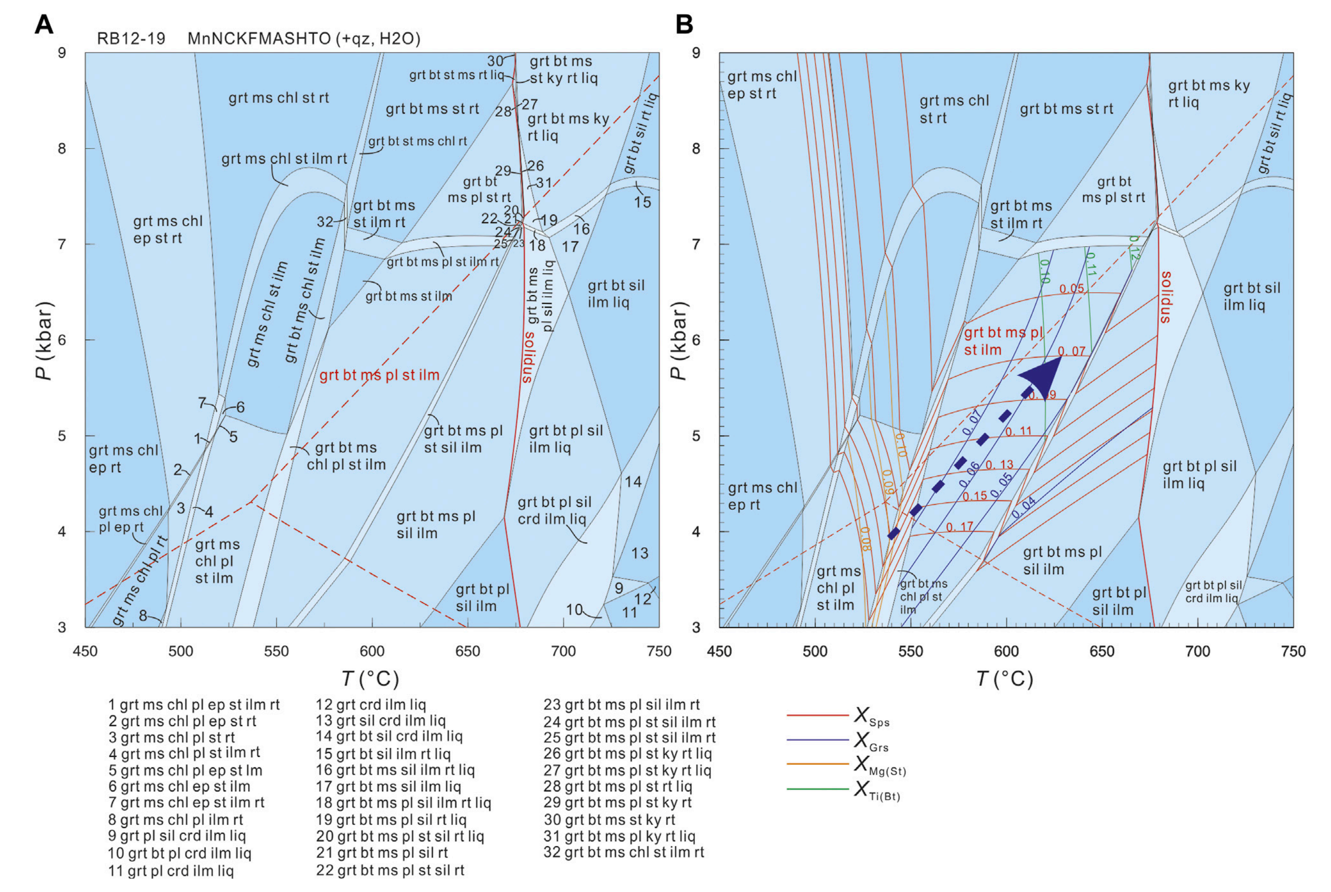

FIGURE 7 | *P–T* pseudosections for the garnet–staurolite–two-mica schist sample RB12-19. **(A)** *P–T* pseudosection that shows mineral assemblages. **(B)** *P–T* pseudosection with isopleths of X_{Sps} and X_{Grs} in garnet, X_{Mg} in staurolite, and X_{Ti} in biotite. The field of peak mineral assemblage is marked by grt–bt–ms–pl–st–ilm–qz–H_2O in red type.

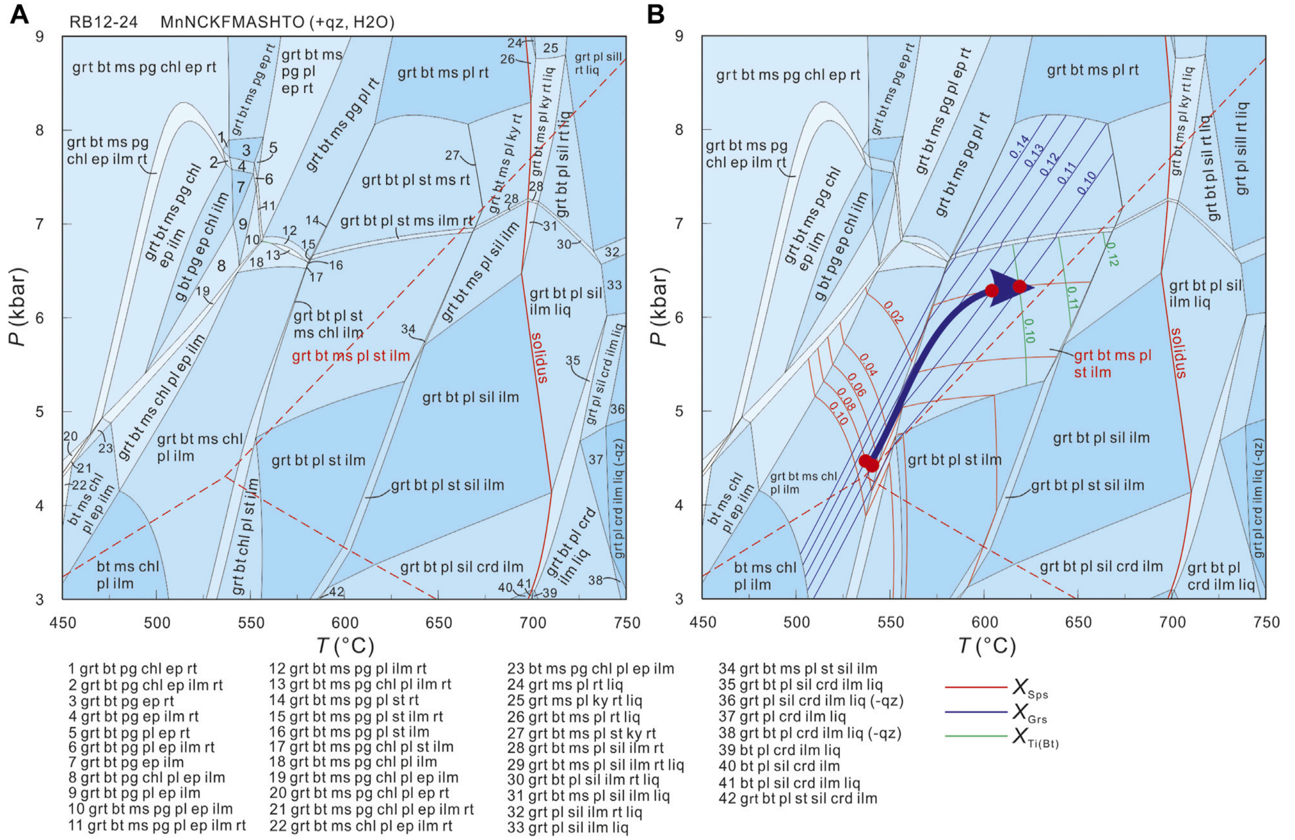

FIGURE 8 | *P–T* pseudosections for the garnet–staurolite–two-mica schist sample RB12-24. **(A)** *P–T* pseudosection that shows mineral assemblages. **(B)** *P–T* pseudosection with isopleths of X_{Sps} and X_{Grs} in garnet and X_{Ti} in biotite. The field of peak mineral assemblage is marked by grt–bt–ms–pl–st–ilm–qz–H_2O in red type.

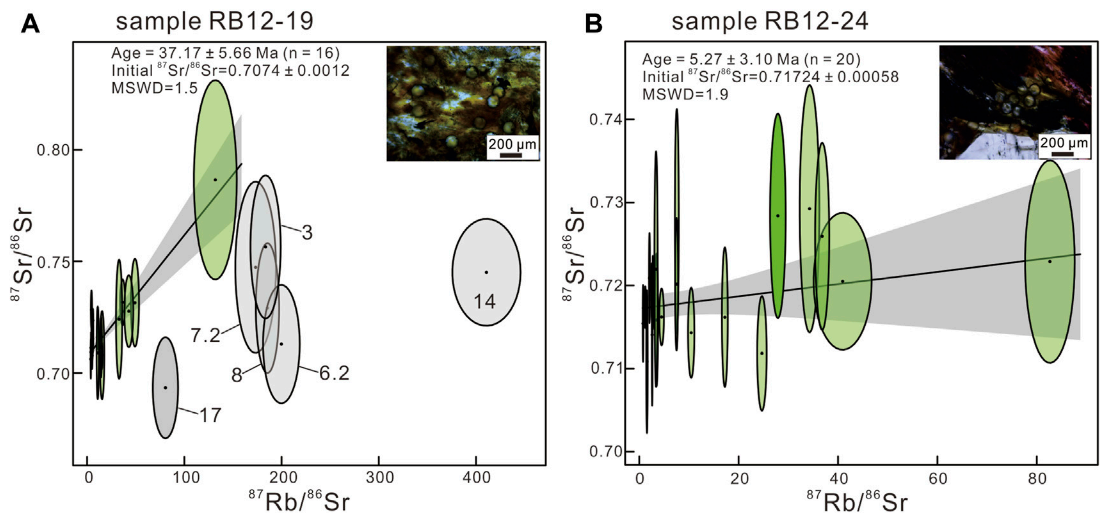

FIGURE 9 | *In situ* LA–ICP–MS biotite Rb–Sr isochron diagrams and photos of biotite with the laser spot: **(A)** sample RB12-19 and **(B)** sample RB12-24.

to 82.637 and 0.711 to 0.729, respectively (**Table 2**). On the $^{87}Rb/^{86}Sr$ and $^{87}Sr/^{86}Sr$ isochron diagram, these data yielded an isochron age of 5.27 ± 3.10 Ma (n = 20, MSWD = 1.9) (**Figure 9B**). Obviously, this age is younger than that of sample RB12-19, although samples RB12-19 and RB12-24 were collected at the same outcrop, which may be due to

TABLE 2 | LA–ICP–MS biotite Rb–Sr data for the garnet–staurolite–two-mica schist samples RB12-19 and RB12-24 of the Ramba gneiss dome.

Spot number	$^{87}Rb/^{86}Sr$	±1σ	$^{87}Sr/^{86}Sr$	±1σ
RB12-19-1.1	4.1439	0.1594	0.7094	0.0024
RB12-19-1.2	5.0593	0.3273	0.7148	0.0041
RB12-19-1.3	3.7942	0.0793	0.7062	0.0036
RB12-19-1.4	15.367	0.931	0.7080	0.0081
RB12-19-2	10.427	0.168	0.7160	0.0023
RB12-19-3	183.523	6.350	0.7565	0.0131
RB12-19-4	49.214	1.695	0.7315	0.0080
RB12-19-5	36.497	1.044	0.7317	0.0042
RB12-19-6.1	10.901	0.480	0.7090	0.0085
RB12-19-6.2	199.794	7.703	0.7130	0.0108
RB12-19-7.1	42.885	1.879	0.7277	0.0066
RB12-19-7.2	173.306	8.544	0.7473	0.0157
RB12-19-8	185.504	4.893	0.7291	0.0119
RB12-19-9	5.0690	0.1682	0.7078	0.0025
RB12-19-10	32.900	1.311	0.7241	0.0109
RB12-19-11	4.0210	0.0361	0.7113	0.0028
RB12-19-12	131.847	9.011	0.7866	0.0182
RB12-19-13	5.8127	0.2173	0.7153	0.0026
RB12-19-14	410.698	14.332	0.7451	0.0098
RB12-19-15	15.153	0.254	0.7078	0.0025
RB12-19-16	4.4781	0.2512	0.7283	0.0035
RB12-19-17	80.555	5.304	0.6933	0.0093
RB12-19-18	5.9343	0.1505	0.7236	0.0021
RB12-19-19	14.368	0.379	0.7115	0.0055
RB12-24-1	27.899	0.641	0.7284	0.0050
RB12-24-2	1.5530	0.0572	0.7108	0.0035
RB12-24-3	82.637	2.040	0.7229	0.0050
RB12-24-4	34.271	0.808	0.7292	0.0061
RB12-24-5	17.226	0.240	0.7162	0.0034
RB12-24-6	10.454	0.259	0.7143	0.0022
RB12-24-7	2.5290	0.0367	0.7194	0.0013
RB12-24-8	0.7626	0.0269	0.7154	0.0019
RB12-24-9	7.5576	0.1586	0.7277	0.0055
RB12-24-10	3.4705	0.1246	0.7159	0.0033
RB12-24-11	40.928	2.385	0.7205	0.0034
RB12-24-12	4.4946	0.1882	0.7162	0.0014
RB12-24-13	24.686	0.388	0.7118	0.0028
RB12-24-14	36.808	0.581	0.7259	0.0046
RB12-24-15	2.5997	0.0296	0.7141	0.0035
RB12-24-16	1.1962	0.0594	0.7174	0.0010
RB12-24-17.1	2.7469	0.0475	0.7192	0.0018
RB12-24-17.2	7.5095	0.1211	0.7202	0.0033
RB12-24-18	2.0603	0.0360	0.7209	0.0022

limited spot analyses for each sample. In fact, sample RB12-19 has two Rb–Sr isotopic trends (**Figure 9A**). The first trend yielded an age of 37.17 ± 5.66 Ma, whereas the second trend did not yield believable age due to the lack of low $^{87}Rb/^{86}Sr$ data (**Figure 9A**). We found that if the Rb–Sr data within the second trend of sample RB12-19 were pooled together with the data of sample RB12-24, they could give a young age of 4.99 ± 1.30 Ma (not shown), with a small error.

DISCUSSION

Age of Metamorphism

Previous dating on Barrow-type metamorphic rocks in the NHGD generally yielded Oligocene to Miocene ages (Stearns et al., 2013; Wang et al., 2018). For example, LA–ICP–MS monazite U/Th-Pb analysis constrained the timing of metamorphism to be 29–14 Ma for grt + bt ± st ± ky ± sil schists from the Kangmar and Mabja gneiss domes (Stearns et al., 2013), and SHRIMP monazite U/Th-Pb analysis yielded ages of ca. 18 Ma for grt + bt + st ± ky ± sil schists in the Yardoi gneiss dome (Wang et al., 2018). These ages were interpreted as the timing of peak Barrow metamorphism recorded in the NHGD (Stearns et al., 2013; Wang et al., 2018), whereas prograde metamorphism occurred as early as 54–49 Ma based on garnet Lu–Hf analysis (Smit et al., 2014). In addition, monazite U/Th-Pb geochronology of the Gianbul dome in the GHC yielded both Eocene (37–33 Ma) and Miocene (26–22 Ma) ages, which were interpreted as the timing of prograde Barrovian metamorphism and doming driven by upper-crustal extension and positive buoyancy of decompression melts, respectively (Horton et al., 2015).

In this study, *in situ* LA–ICP–MS biotite Rb–Sr dating yielded two metamorphic ages of 37.17 ± 5.66 and 5.27 ± 3.10 Ma for the garnet–staurolite–two-mica schist in the Ramba gneiss dome (**Figure 9**). As the peak metamorphic temperatures of the garnet–staurolite–two-mica schists in the Ramba gneiss dome are higher than the closure temperature of the Rb–Sr system in biotite (~300–400°C) (Verschure et al., 1980; Willigers et al., 2004 and references therein; Scibiorski et al., 2021), the age of 37.17 ± 5.66 Ma is interpreted to represent the timing of retrograde cooling, rather than the peak metamorphism. This interpretation is obviously inconsistent with results from the Kangmar, Mabja, and Yardoi gneiss domes in the Northern Himalayas and the Gianbul dome in the GHC. However, Laskowski et al. (2016) have conducted geochronological research on HP meta-Tethyan rocks in the Lopu Range, located ~600 km west of the city of Lhasa, yielding a garnet Lu-Hf age of 40.4 ± 1.4 Ma and five Ar-Ar phengite ages between 39 and 34 Ma, which were interpreted as the timing of prograde metamorphism and exhumation to mid-crustal depths (~25 km) and concomitant retrogression in the Himalayan orogen, respectively. Khanal et al. (2021) presented new monazite petrochronology for the Kathmandu Klippe in the central Nepalese Himalayas and revealed that Eocene prograde metamorphism and partial melting occurred at 44–38 Ma and 38–35 Ma, respectively (**Figure 10**). Although the meta-Tethyan rocks in the Lopu Range underwent HP metamorphism and the Kathmandu Klippe belong to the upper or uppermost Greater Himalayan Crystallines, these results support that part of the middle-to-lower crustal rocks in the Himalayan orogen underwent exhumation and were not overprinted by Oligocene to Miocene peak Barrow metamorphism.

The age of 5.27 ± 3.10 Ma is significantly younger than the crystallization ages (ca. 44 Ma and ca. 28 Ma) of granitic rocks that intruded into the margin of the Ramba gneiss dome (Liu et al., 2014, 2019). However, this age is slightly younger than the crystallization age (ca. 8 Ma) of the leucogranite pluton occupying the core of the dome (Liu et al., 2014) but is similar to $^{40}Ar/^{39}Ar$ cooling ages (ca. 6 Ma) of the leucogranite pluton (Guo et al., 2008). Therefore, the age of 5.27 ± 3.10 Ma is

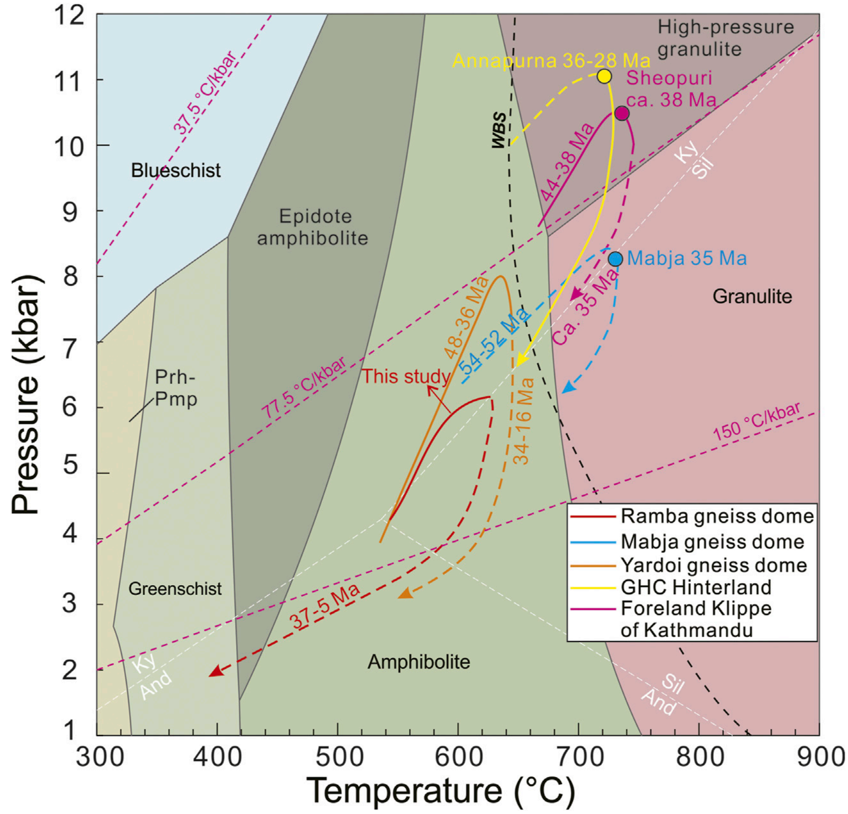

FIGURE 10 | Summary of *P–T–t* paths of different Eocene units across the Himalayas, including the Ramba gneiss dome in this study, the Majba gneiss dome (Lee et al., 2004; Lee and Whitehouse, 2007; Smit et al., 2014), the Yardoi gneiss dome (Ding et al., 2016b), Hinterland GHC (Iaccarino et al., 2015), and the Kathmandu Klippe (Khanal et al., 2021). The boundary lines for metamorphic facies are modified from Palin et al. (2020). UHT—ultrahigh temperature; WBS—wet basalt solidus.

considered to represent the cooling age of the dome, following the emplacement of the ca. 8 Ma leucogranites.

Metamorphic P–T Paths

In this study, we have determined *P–T* paths for the garnet–staurolite–two-mica schists in the Ramba gneiss dome (**Figures 7B**, **8B**). Sample RB12-19 recorded a prograde *P–T* path that evolves roughly from ~540°C at ~4 kbar to ~630°C at ~5.8 kbar (**Figure 7B**). The prograde *P–T* path for sample RB12-24 evolves from ~540°C at ~4.4 kbar to ~620°C at ~6.3 kbar (**Figure 8B**), which displays a slightly higher temperature than those of sample RB12-19 at similar pressure (**Figures 7B**, **8**). When the results of the two samples are combined, it is clear that they experienced an obviously early heating burial path (**Figure 10**). It can be noted that sample RB12-24 recorded a nearly isobaric heating path (**Figure 8B**), and thus, a clock-wise *P–T* evolution is inferred to the garnet–staurolite–two-mica schist in the Ramba gneiss dome (**Figure 10**).

Here, we compared this *P–T* path with those retrieved from the Mabja and Yardoi gneiss domes in the northern Himalaya, the hinterland GHC, and the foreland Kathmandu Klippe (**Figure 10**). The migmatite sample of the sillimanite zone in the Mabja gneiss dome has a peak metamorphic condition of 8.2 kbar/705°C (Lee et al., 2004), which is higher in both pressure and temperature than those of the garnet–staurolite–two-mica schist in the Ramba gneiss dome (**Figure 10**). The garnet–staurolite–kyanite schist in the Yardoi gneiss dome has a peak metamorphic mineral assemblage of grt-bt-ms-pl-st-ky-ilm-qz, occurring in a narrow *P–T* condition of 7.2–8.0 kbar and 640–645°C, and the prograde *P–T* condition was constrained to be ~540°C at ~4.6 kbar using compositional isopleths X_{Mg} (0.07) and X_{Mn} (0.17) of the garnet core (Ding et al., 2016b). Combined with the retrograde metamorphic process constrained using the occurrence of sillimanite and biotite in the shear bands and the presence of chlorite, Ding et al. (2016b) obtained a clockwise *P–T* path for the garnet–staurolite–kyanite schist in the Yardoi gneiss dome, which is similar to that constrained by Wang et al. (2018). This *P–T* path is characterized by a prograde process with both P and T increasing and a retrograde process with an early nearly isothermal decompression and late cooling and decompression. It is obvious that the garnet–staurolite–two-mica schist in the Ramba gneiss dome has a similar prograde *P–T* condition to that of the schist in the Yardoi gneiss dome but a lower pressure condition at P_{max} (**Figure 10**). In this study, the retrograde *P–T* evolution was not supported by the petrological evidence and was only inferred. The *P–T* path of the Kathmandu

Klippe in the central Nepalese Himalayas is clockwise, with peak P–T conditions of 730–760°C and up to 10.5 kbar, which is higher in both pressure and temperature than those of the garnet–staurolite–two-mica schist in the Ramba gneiss dome but is similar to those from the GHC hinterland (**Figure 10**) (Iaccarino et al., 2015).

Implications for the Formation of the Ramba Gneiss Dome

Ultrahigh pressure (UHP) metamorphic rocks at Kaghan Valley and Tso Morari in the west of the northern Himalayan belt have peak metamorphic ages of 46.2 ± 0.7 Ma and ca. 47–43 Ma, respectively (Kaneko et al., 2003; Donaldson et al., 2013). These suggest deep subduction of the Indian continent at ca. 47–43 Ma. The crustal thickening in the Tibetan Himalaya is broadly synchronous with the Eocene collision between the Indian and Asian plates (Smit et al., 2014). Following the crustal thickening, the deeply buried Indian continental crust underwent a long-lived partial melting (Wang et al., 2013; Zhang et al., 2015), which formed the ca. 48 to 8 Ma granites or leucogranites in the northern Himalayan belt (Aikman et al., 2008; Zhang et al., 2012; Liu et al., 2014; Zeng et al., 2011; Gao et al., 2012; Wu et al., 2015; Zeng and Gao, 2017 and references). In the Ramba gneiss dome, the partial melting is reflected by three epidotes (ca. 44 Ma, ca. 28 Ma, and ca. 8 Ma) of granitic magmatism (Liu et al., 2014, 2019). On the basis of the similarities in Eocene metamorphic conditions and timing of anatexis in the different Eocene units across the Himalayas, Khanal et al. (2021) concluded that an early-stage anatectic response to crustal thickening might be more common than previously thought.

The onset of extensional tectonics of the STDS occurred as early as ca. 36–30 Ma, which marks the initial thinning of thickened crust in the northern Himalayan belt (Zhang et al., 2012; La Roche et al., 2016). In the Ramba gneiss dome, the STDS is represented by the first episode of deformation with top to-NNW sliding, indicated by S–C fabric and NNW-convergent tight folds on the northwestern flank of the dome (Guo et al., 2008; Zhang et al., 2012). The clock-wise P–T evolution of the garnet–staurolite–two-mica schist in the Ramba gneiss dome, combined with the age of 37.17 ± 5.66 Ma from the *in situ* LA–ICP–MS biotite Rb–Sr dating, is consistent with the Eocene crustal thickening (**Figure 10**).

The ca. 8 Ma leucogranites occupy the core of the Ramba gneiss dome (Liu et al., 2014) and have $^{40}Ar/^{39}Ar$ cooling ages of ca. 6 Ma (Guo et al., 2008). The Yadong–Gulu rift, on the east of the dome, was active during the interval ca. 11–5 Ma, with its peak activity at ca. 8 Ma (Pan and Kidd, 1992; Harrison et al., 1995; Zhang et al., 2012), which coincides with the diapir of the ca. 8 Ma leucogranite pluton, formed the shape of the Ramba gneiss dome (Guo et al., 2008; Zhang et al., 2012; Liu et al., 2014).

CONCLUSION

The garnet–staurolite–two-mica schist in the Ramba gneiss dome followed a clock-wise P–T path, involving an early prograde process that evolves from ~540°C at ~4.4 kbar to ~630°C at ~6.0 kbar. This prograde evolution is similar to the schist in the Yardoi gneiss dome but with lower T condition at P_{max} and reflects the crustal thickening, following the Indian-Asian collision. *In situ* LA–ICP–MS biotite Rb–Sr analysis obtained two metamorphic ages of 37.17 ± 5.66 and 5.27 ± 3.10 Ma for the garnet–staurolite–two-mica schist in the Ramba gneiss dome. The former corresponds to the timing of retrograde cooling. The latter is similar to $^{40}Ar/^{39}Ar$ cooling ages (ca. 6 Ma) of ca. 8 Ma leucogranite and, thus, represents the cooling age of the dome, following the thermal resetting by the emplacement of ca. 8 Ma leucogranite pluton in the core of the dome. The peak metamorphism should be older than ca. 37 Ma.

DATA AVAILABILITY STATEMENT

The original contributions presented in the study are included in the article/**Supplementary Material**; further inquiries can be directed to the corresponding author.

AUTHOR CONTRIBUTIONS

L-LG: investigation, data curation, and writing—original draft preparation. X-PL: conceptualization and investigation. H-YY, T-CS, and J-YW: investigation. X-FX, FZ, and Z-BT: visualization and editing.

FUNDING

This work is supported by a research grant from the State Key Laboratory of Continental Dynamics (SKLCD-04).

ACKNOWLEDGMENTS

The authors thank editor YC for editorial handling work. HW and J-MW for their helpful comments that significantly improved the manuscript.

SUPPLEMENTARY MATERIAL

The Supplementary Material for this article can be found online at: https://www.frontiersin.org/articles/10.3389/feart.2022.887154/full#supplementary-material

REFERENCES

Aikman, A. B., Harrison, T. M., and Lin, D. (2008). Evidence for Early (>44 Ma) Himalayan Crustal Thickening, Tethyan Himalaya, Southeastern Tibet. *Earth Planet. Sci. Lett.* 274, 14–23. doi:10.1016/j.epsl.2008.06.038

Aoya, M., Wallis, S. R., Kawakami, T., Lee, J., Wang, Y., and Maeda, H. (2006). The Malashan Gneiss Dome in South Tibet: Comparative Study with the Kangmar Dome with Special Reference to Kinematics of Deformation and Origin of Associated Granites. *Geol. Soc. Lond. Spec. Publ.* 268, 471–495. doi:10.1144/gsl.sp.2006.268.01.22

Beaumont, C., Jamieson, R. A., Nguyen, M. H., and Lee, B. (2001). Himalayan Tectonics Explained by Extrusion of a Low-Viscosity Crustal Channel Coupled to Focused Surface Denudation. *Nature* 414, 738–742. doi:10.1038/414738a

Chen, Z., Liu, Y., Hodges, K. V., Burchfiel, B. C., Royden, L. H., and Deng, C. (1990). The Kangmar Dome: A Metamorphic Core Complex in Southern Xizang (Tibet). *Science* 250, 1552–1556. doi:10.1126/science.250.4987.1552

Ding, H., Zhang, Z., Dong, X., Tian, Z., Xiang, H., Mu, H., et al. (2016a). Early Eocene (C . 50 Ma) Collision of the Indian and Asian Continents: Constraints from the North Himalayan Metamorphic Rocks, Southeastern Tibet. *Earth Planet. Sci. Lett.* 435, 64–73. doi:10.1016/j.epsl.2015.12.006

Ding, H., Zhang, Z., Hu, K., Dong, X., Xiang, H., and Mu, H. (2016b). P-T-t-D Paths of the North Himalayan Metamorphic Rocks: Implications for the Himalayan Orogeny. *Tectonophysics* 683, 393–404. doi:10.1016/j.tecto.2016.06.035

Donaldson, D. G., Webb, A. A. G., Menold, C. A., Kylander-Clark, A. R. C., and Hacker, B. R. (2013). Petrochronology of Himalayan Ultrahigh-Pressure Eclogite. *Geology* 41, 835–838. doi:10.1130/g33699.1

Fu, J., Li, G., Wang, G., Huang, Y., Zhang, L., Dong, S., et al. (2016). First Field Identification of the Cuonadong Dome in Southern Tibet: Implications for EW Extension of the North Himalayan Gneiss Dome. *Int. J. Earth Sci. Geol. Rundsch)* 106, 1581–1596. doi:10.1007/s00531-016-1368-2

Gao, L., Zeng, L., and Xie, K. (2012). Eocene High Grade Metamorphism and Crustal Anatexis in the North Himalaya Gneiss Domes, Southern Tibet,Southern Tibet. *Chin. Sci. Bull.* 57, 639–650. doi:10.1007/s11434-011-4805-4

Gorojovsky, L., and Alard, O. (2020). Optimisation of Laser and Mass Spectrometer Parameters for the *In Situ* Analysis of Rb/Sr Ratios by LA-ICP-MS/MS. *J. Anal. At. Spectrom.* 35, 2322–2336. doi:10.1039/d0ja00308e

Gou, Z., Zhang, Z., Dong, X., Xiang, H., Ding, H., Tian, Z., et al. (2016). Petrogenesis and Tectonic Implications of the Yadong Leucogranites, Southern Himalaya. *Lithos* 256-257, 300–310. doi:10.1016/j.lithos.2016.04.009

Guo, L., Zhang, J., and Zhang, B. (2008). Structures, Kinematics, Thermochronology and Tectonic Evolution of the Ramba Gneiss Dome in the Northern Himalaya. *Prog. Nat. Sci.* 18, 851–860. doi:10.1016/j.pnsc.2008.01.016

Harris, N. (2007). Channel Flow and the Himalayan-Tibetan Orogen: a Critical Review. *J. Geol. Soc.* 164, 511–523. doi:10.1144/0016-76492006-133

Harrison, T. M., Copeland, P., Kidd, W. S. F., and Lovera, O. M. (1995). Activation of the Nyainqentanghla Shear Zone: Implications for Uplift of the Southern Tibetan Plateau. *Tectonics* 14, 658–676. doi:10.1029/95tc00608

Hogmalm, K. J., Zack, T., Karlsson, A. K.-O., Sjöqvist, A. S. L., and Garbe-Schönberg, D. (2017). *In Situ* Rb-Sr and K-Ca Dating by LA-ICP-MS/MS: an Evaluation of N2O and SF6 as Reaction Gases. *J. Anal. At. Spectrom.* 32, 305–313. doi:10.1039/c6ja00362a

Holland, T. J. B., and Powell, R. (2011). An Improved and Extended Internally Consistent Thermodynamic Dataset for Phases of Petrological Interest, Involving a New Equation of State for Solids. *J. Metamorph. Geol.* 29, 333–383. doi:10.1111/j.1525-1314.2010.00923.x

Holland, T., and Powell, R. (2003). Activity?composition Relations for Phases in Petrological Calculations: an Asymmetric Multicomponent Formulation. *Contributions Mineralogy Petrology* 145, 492–501. doi:10.1007/s00410-003-0464-z

Hopkinson, T. N., Harris, N. B. W., Warren, C. J., Spencer, C. J., Roberts, N. M. W., Horstwood, M. S. A., et al. (2017). The Identification and Significance of Pure Sediment-Derived Granites. *Earth Planet. Sci. Lett.* 467, 57–63. doi:10.1016/j.epsl.2017.03.018

Horton, F., Lee, J., Hacker, B., Bowman-Kamaha'o, M., and Cosca, M. (2015). Himalayan Gneiss Dome Formation in the Middle Crust and Exhumation by Normal Faulting: New Geochronology of Gianbul Dome, Northwestern India. *Geol. Soc. Am. Bull.* 127, 162–180. doi:10.1130/b31005.1

Iaccarino, S., Montomoli, C., Carosi, R., Massonne, H.-J., Langone, A., and Visonà, D. (2015). Pressure-temperature-time-deformation Path of Kyanite-Bearing Migmatitic Paragneiss in the Kali Gandaki Valley (Central Nepal): Investigation of Late Eocene-Early Oligocene Melting Processes. *Lithos* 231, 103–121. doi:10.1016/j.lithos.2015.06.005

Iaccarino, S., Montomoli, C., Carosi, R., Massonne, H.-J., and Visonà, D. (2017). Geology and Tectono-Metamorphic Evolution of the Himalayan Metamorphic Core: Insights from the Mugu Karnali Transect, Western Nepal (Central Himalaya). *J. Metamorph. Geol.* 35, 301–325. doi:10.1111/jmg.12233

Jessup, M. J., Langille, J. M., Diedesch, T. F., and Cottle, J. M. (2019). Gneiss Dome Formation in the Himalaya and Southern Tibet. *Geol. Soc. Lond. Spec. Publ.* 483 (1), 401–422. doi:10.1144/sp483.15

Kaneko, Y., Katayama, I., Yamamoto, H., Misawa, K., Ishikawa, M., Rehman, H. U., et al. (2003). Timing of Himalayan Ultrahigh-Pressure Metamorphism: Sinking Rate and Subduction Angle of the Indian Continental Crust beneath Asia. *J. Metamorph Geol.* 21, 589–599. doi:10.1046/j.1525-1314.2003.00466.x

Khanal, G. P., Wang, J. M., Larson, K. P., Wu, F. Y., Rai, S. M., Wang, J. G., et al. (2021). Eocene Metamorphism and Anatexis in the Kathmandu Klippe, Central Nepal: Implications for Early Crustal Thickening and Initial Rise of the Himalaya. *Tectonics* 40, e2020TC006532. doi:10.1029/2020tc006532

Kohn, M. J., and Corrie, S. L. (2011). Preserved Zr-Temperatures and U-Pb Ages in High-Grade Metamorphic Titanite: Evidence for a Static Hot Channel in the Himalayan Orogen. *Earth Planet. Sci. Lett.* 311, 136–143. doi:10.1016/j.epsl.2011.09.008

La Roche, R. S., Godin, L., Cottle, J. M., and Kellett, D. A. (2016). Direct Shear Fabric Dating Constrains Early Oligocene Onset of the South Tibetan Detachment in the Western Nepal Himalaya. *Geology* 44, 403–406. doi:10.1130/g37754.1

Laskowski, A. K., Kapp, P., Vervoort, J. D., and Ding, L. (2016). High-pressure Tethyan Himalaya Rocks along the India-Asia Suture Zone in Southern Tibet. *Lithosphere* 8, 574–582. doi:10.1130/l544.1

Le Fort, P., Cuney, M., Deniel, C., France-Lanord, C., Sheppard, S. M. F., Upreti, B. N., et al. (1987). Crustal Generation of the Himalayan Leucogranites. *Tectonophysics* 134, 39–57. doi:10.1016/0040-1951(87)90248-4

Lee, J., Hacker, B. R., Dinklage, W. S., Wang, Y., Gans, P., Calvert, A., et al. (2000). Evolution of the Kangmar Dome, Southern Tibet: Structural, Petrologic, and Thermochronologic Constraints. *Tectonics* 19, 872–895. doi:10.1029/1999tc001147

Lee, J., Hacker, B., and Wang, Y. (2004). Evolution of North Himalayan Gneiss Domes: Structural and Metamorphic Studies in Mabja Dome, Southern Tibet. *J. Struct. Geol.* 26, 2297–2316. doi:10.1016/j.jsg.2004.02.013

Lee, J., McClelland, W., Wang, Y., Blythe, A., and McWilliams, M. (2006). Oligocene-Miocene Middle Crustal Flow in Southern Tibet: Geochronology of Mabja Dome. *Geol. Soc. Lond. Spec. Publ.* 268, 445–469. doi:10.1144/gsl.sp.2006.268.01.21

Lee, J., and Whitehouse, M. J. (2007). Onset of Mid-crustal Extensional Flow in Southern Tibet: Evidence from U/Pb Zircon Ages. *Geol* 35, 45–48. doi:10.1130/g22842a.1

Li, Q., Zhang, L., Fu, B., Bader, T., and Yu, H. (2019). Petrology and Zircon U-Pb Dating of Well-preserved Eclogites from the Thongmön Area in Central Himalaya and Their Tectonic Implications. *J. Metamorph Geol.* 37, 203–226. doi:10.1111/jmg.12457

Lister, G. S., and Davis, G. A. (1989). The Origin of Metamorphic Core Complexes and Detachment Faults Formed during Tertiary Continental Extension in the Northern Colorado River Region, U.S.A. *J. Struct. Geol.* 11, 65–94. doi:10.1016/0191-8141(89)90036-9

Liu, S., Zhang, G., Zhang, L., Liu, Z., and Xu, J. (2022a). Boron Isotopes of Tourmalines from the Central Himalaya: Implications for Fluid Activity and Anatexis in the Himalayan Orogen. *Chem. Geol.* 596, 120800. doi:10.1016/j.chemgeo.2022.120800

Liu, S., Zhang, G., Zhang, L., Wang, S., Upreti, B. N., Adhikari, D. P., et al. (2022b). Diverse Anatexis in the Main Central Thrust Zone, Eastern Nepal: Implications for Melt Evolution and Exhumation Process of the Himalaya. *J. Petrology* 63 (3), 1–26. doi:10.1093/petrology/egac003

Liu, Z.-C., Wu, F.-Y., Ji, W.-Q., Wang, J.-G., and Liu, C.-Z. (2014). Petrogenesis of the Ramba Leucogranite in the Tethyan Himalaya and Constraints on the Channel Flow Model. *Lithos* 208-209, 118–136. doi:10.1016/j.lithos.2014.08.022

Liu, Z.-C., Wu, F.-Y., Liu, X.-C., Wang, J.-G., Yin, R., Qiu, Z.-L., et al. (2019). Mineralogical Evidence for Fractionation Processes in the Himalayan Leucogranites of the Ramba Dome, Southern Tibet. *Lithos* 340-341, 71–86. doi:10.1016/j.lithos.2019.05.004

Mark Harrison, T., Lovera, O. M., and Grove, M. (1997). New Insights into the Origin of Two Contrasting Himalayan Granite Belts. *Geol* 25, 899–902. doi:10.1130/0091-7613(1997)025<0899:niitoo>2.3.co;2

Palin, R. M., Santosh, M., Cao, W., Li, S.-S., Hernández-Uribe, D., and Parsons, A. (20202020). Secular Change and the Onset of Plate Tectonics on Earth. *Earth-Science Rev.* 207, 103172. doi:10.1016/j.earscirev.2020.103172

Palin, R. M., Searle, M. P., St-Onge, M. R., Waters, D. J., Roberts, N. M. W., Horstwood, M. S. A., et al. (2014). Monazite Geochronology and Petrology of Kyanite- and Sillimanite-Grade Migmatites from the Northwestern Flank of the Eastern Himalayan Syntaxis. *Gondwana Res.* 26, 323–347. doi:10.1016/j.gr.2013.06.022

Pan, Y., and Kidd, W. S. F. (1992). Nyainqentanglha Shear Zone: A Late Miocene Extensional Detachment in the Southern Tibetan Plateau. *Geol* 20, 775–778. doi:10.1130/0091-7613(1992)020<0775:nszalm>2.3.co;2

Powell, R., Holland, T., and Worley, B. (1998). Calculating Phase Diagrams Involving Solid Solutions via Non-linear Equations, with Examples Using THERMOCALC. *J. Metamorph. Geol.* 16, 577–588. doi:10.1111/j.1525-1314.1998.00157.x

Quigley, M. C., Liangjun, Y., Gregory, C., Corvino, A., Sandiford, M., Wilson, C. J. L., et al. (2008). U-pb SHRIMP Zircon Geochronology and T-T-D History of the Kampa Dome, Southern Tibet. *Tectonophysics* 446, 97–113. doi:10.1016/j.tecto.2007.11.004

Regis, D., Warren, C. J., Young, D., and Roberts, N. M. W. (2014). Tectono-metamorphic Evolution of the Jomolhari Massif: Variations in Timing of Syn-Collisional Metamorphism across Western Bhutan. *Lithos* 190-191, 449–466. doi:10.1016/j.lithos.2014.01.001

Rey, P. F., Mondy, L., Duclaux, G., Teyssier, C., Whitney, D. L., Bocher, M., et al. (2017). The Origin of Contractional Structures in Extensional Gneiss Domes. *Geology* 45, 263–266. doi:10.1130/g38595.1

Scibiorski, E., Jourdan, F., Mezger, K., Tohver, E., and Vollstaedt, H. (2021). Cryptic Excess Argon in Metamorphic Biotite: Anomalously Old 40Ar/39Ar Plateau Dates Tested with Rb/Sr Thermochronology and Ar Diffusion Modelling. *Geochimica Cosmochimica Acta* 315, 1–23. doi:10.1016/j.gca.2021.09.017

Searle, M. P., Cottle, J. M., Streule, M. J., and Waters, D. J. (2009). Crustal Melt Granites and Migmatites along the Himalaya: Melt Source, Segregation, Transport and Granite Emplacement Mechanisms. *Earth Environ. Sci. Trans. R. Soc. Edinb.* 100, 219–233. doi:10.1017/s175569100901617x

Searle, M. P., and Godin, L. (2003). The South Tibetan Detachment and the Manaslu Leucogranite: A Structural Reinterpretation and Restoration of the Annapurna-Manaslu Himalaya, Nepal. *J. Geol.* 111, 505–523. doi:10.1086/376763

Searle, M. P., Noble, S. R., Hurford, A. J., and Rex, D. C. (1999). Age of Crustal Melting, Emplacement and Exhumation History of the Shivling Leucogranite, Garhwal Himalaya. *Geol. Mag.* 136, 513–525. doi:10.1017/s0016756899002885

Shrestha, S., Larson, K. P., Guilmette, C., and Smit, M. A. (2017). The P-T-T Evolution of the Exhumed Himalayan Metamorphic Core in the Likhu Khola Region, East Central Nepal. *J. Metamorph Geol.* 35, 663–693. doi:10.1111/jmg.12250

Smit, M. A., Hacker, B. R., and Lee, J. (2014). Tibetan Garnet Records Early Eocene Initiation of Thickening in the Himalaya. *Geology* 42, 591–594. doi:10.1130/g35524.1

Smye, A. J., Greenwood, L. V., and Holland, T. J. B. (2010). Garnet-chloritoid-kyanite Assemblages: Eclogite Facies Indicators of Subduction Constraints in Orogenic Belts. *Geology* 28, 753–768. doi:10.1111/j.1525-1314.2010.00889.x

Stearns, M. A., Hacker, B. R., Ratschbacher, L., Lee, J., Cottle, J. M., and Kylander-Clark, A. (2013). Synchronous Oligocene-Miocene Metamorphism of the Pamir and the North Himalaya Driven by Plate-Scale Dynamics. *Geology* 41, 1071–1074. doi:10.1130/g34451.1

Teyssier, C., and Whitney, D. L. (2002). Gneiss Domes and Orogeny. *Geol* 30, 1139–1142. doi:10.1130/0091-7613(2002)030<1139:gdao>2.0.co;2

Tian, Z., Zhang, Z., and Dong, X. (2019). Constraining the Age of High-Pressure Metamorphism of Paragneisses from the Eastern Himalayan Syntaxis Using Zircon Petrochronology and Phase Equilibria. *Geol. Soc. Lond. Spec. Publ.* 474, 331–352. doi:10.1144/sp474.11

Verschure, R. H., Andriessen, P. A. M., Boelrijk, N. A. I. M., Hebeda, E. H., Maijer, C., Priem, H. N. A., et al. (1980). On the Thermal Stability of Rb-Sr and K-Ar Biotite Systems: Evidence from Coexisting Sveconorwegian (Ca 870 Ma) and Caledonian (Ca 400 Ma) Biotites in SW Norway. *Contr. Mineral. Pet.* 74, 245–252. doi:10.1007/bf00371694

Wang, J.-M., Lanari, P., Wu, F.-Y., Zhang, J.-J., Khanal, G. P., and Yang, L. (2021). First Evidence of Eclogites Overprinted by Ultrahigh Temperature Metamorphism in Everest East, Himalaya: Implications for Collisional Tectonics on Early Earth. *Earth Planet. Sci. Lett.* 558, 116760. doi:10.1016/j.epsl.2021.116760

Wang, J.-M., Rubatto, D., and Zhang, J.-J. (2015). Timing of Partial Melting and Cooling across the Greater Himalayan Crystalline Complex (Nyalam, Central Himalaya): In-Sequence Thrusting and its Implications. *J. Petrol.* 56, 1677–1702. doi:10.1093/petrology/egv050

Wang, J.-M., Wu, F.-Y., Rubatto, D., Liu, K., Zhang, J.-J., and Liu, X.-C. (2018). Early Miocene Rapid Exhumation in Southern Tibet: Insights from P-T-T-D-Magmatism Path of Yardoi Dome. *Lithos* 304-307, 38–56. doi:10.1016/j.lithos.2018.02.003

Wang, J.-M., Wu, F.-Y., Rubatto, D., Liu, S.-R., Zhang, J.-J., Liu, X.-C., et al. (2017a). Monazite Behaviour during Isothermal Decompression in Pelitic Granulites: a Case Study from Dinggye, Tibetan Himalaya. *Contrib. Mineral. Pet.* 172, 81. doi:10.1007/s00410-017-1400-y

Wang, J.-M., Zhang, J.-J., Liu, K., Zhang, B., Wang, X.-X., Rai, S., et al. (2016). Spatial and Temporal Evolution of Tectonometamorphic Discontinuities in the Central Himalaya: Constraints from P-T Paths and Geochronology. *Tectonophysics* 679, 41–60. doi:10.1016/j.tecto.2016.04.035

Wang, J. M., Zhang, J. J., and Wang, X. X. (2013). Structural Kinematics, Metamorphic P-T Profiles and Zircon Geochronology across the Greater Himalayan Crystalline Complex in South-Central Tibet: Implication for a Revised Channel Flow. *J. Meta. Geol.* 31, 607–628. doi:10.1111/jmg.12036

Wang, Y., Zhang, L., Zhang, J., and Wei, C. (2017b). The Youngest Eclogite in Central Himalaya: P-T Path, U-Pb Zircon Age and its Tectonic Implication. *Gondwana Res.* 41, 188–206. doi:10.1016/j.gr.2015.10.013

White, R. W., Powell, R., Holland, T. J. B., Johnson, T. E., and Green, E. C. R. (2014a). New Mineral Activity-Composition Relations for Thermodynamic Calculations in Metapelitic Systems. *J. Meta. Geol.* 32, 261–286. doi:10.1111/jmg.12071

White, R. W., Powell, R., Holland, T. J. B., and Worley, B. A. (2000). The Effect of TiO2 and Fe2 O3 on Metapelitic Assemblages at Greenschist and Amphibolite Facies Conditions: Mineral Equilibria Calculations in the System K2 O-FeO-MgO-Al2 O3 -SiO2 -H2 O-TiO2 -Fe2 O3. *J. Metamorph. Geol.* 18, 497–511. doi:10.1046/j.1525-1314.2000.00269.x

White, R. W., Powell, R., and Johnson, T. E. (2014b). The Effect of Mn on Mineral Stability in Metapelites Revisited: New a -x Relations for Manganese-Bearing Minerals. *J. Meta. Geol.* 32, 809–828. doi:10.1111/jmg.12095

Whitney, D. L., and Evans, B. W. (2010). Abbreviations for Names of Rock-Forming Minerals. *Am. Mineralogist* 95, 185–187. doi:10.2138/am.2010.3371

Whitney, D. L., Teyssier, C., and Vanderhaeghe, O. (2004). Gneiss Domes and Crustal Flow. *Geol. Soc. Am. Special Pap.* 380, 15–33. doi:10.1130/0-8137-2380-9.15

Willigers, B. J. A., Mezger, K., and Baker, J. A. (2004). Development of High Precision Rb-Sr Phlogopite and Biotite Geochronology; an Alternative to 40Ar/39Ar Tri-octahedral Mica Dating. *Chem. Geol.* 213, 339–358. doi:10.1016/j.chemgeo.2004.07.006

Woodhead, J. D., and Hergt, J. M. (2001). Strontium, Neodymium and Lead Isotope Analyses of NIST Glass Certified Reference Materials: SRM 610, 612, 614. *Geostand. Newsl.* 25, 261–266. doi:10.1111/j.1751-908x.2001.tb00601.x

Wu, C. G., Zhang, L. F., Li, Q. Y., Bader, T., Wang, Y., and Fu, B. (2022). Tectonothermal Transition from Continental Collision to Post-collision: Insights from Eclogites Overprinted in the Ultrahigh-Temperature Granulite Facies (Yadong Region, Central Himalaya). *J. Metamorph. Geol.*, 1–27.

Wu, F. Y., Liu, Z. C., Liu, X. C., and Ji, W. Q. (2015). Himalayan Leucogranites: Petrogenesis and Implications to Orogenesis and Plateau Uplift. *Acta Petrol. Sin.* 31, 1–36. (in Chinese with English abstract).

Yin, A. (2006). Cenozoic Tectonic Evolution of the Himalayan Orogen as Constrained by Along-Strike Variation of Structural Geometry, Exhumation History, and Foreland Sedimentation. *Earth-Science Rev.* 76, 1–131. doi:10.1016/j.earscirev.2005.05.004

Yin, A. (2004). Gneiss Domes and Gneiss Dome Systems. *Geol. Soc. Am. Special Pap.* 380, 1–14. doi:10.1130/0-8137-2380-9.1

Yin, A., and Harrison, T. M. (2000). Geologic Evolution of the Himalayan-Tibetan Orogen. *Annu. Rev. Earth Planet. Sci.* 28, 211–280. doi:10.1146/annurev.earth.28.1.211

Zeng, L., Gao, L.-E., Xie, K., and Liu-Zeng, J. (2011). Mid-Eocene High Sr/Y Granites in the Northern Himalayan Gneiss Domes: Melting Thickened Lower Continental Crust. *Earth Planet. Sci. Lett.* 303, 251–266. doi:10.1016/j.epsl.2011.01.005

Zeng, L. S., and Gao, L. E. (2017). Cenozoic Crustal Anatexis and the Leucogranites in the Himalayan Collisional Orogenic Belt. *Acta Petrol. Sin.* 33, 1420–1444. (in Chinese with English abstract).

Zhang, G. B., Wang, J. X., Webb, A. A. G., Zhang, L. F., Liu, S. Q., Fu, B., et al. (2021). *The Protoliths of Central Himalayan Eclogites*. Geological Society of America Bulletin. doi:10.1130/B36080.1

Zhang, H., Harris, N., Parrish, R., Kelley, S., Zhang, L., Rogers, N., et al. (2004). Causes and Consequences of Protracted Melting of the Mid-crust Exposed in the North Himalayan Antiform. *Earth Planet. Sci. Lett.* 228, 195–212. doi:10.1016/j.epsl.2004.09.031

Zhang, J., and Guo, L. (2007). Structure and Geochronology of the Southern Xainza-Dinggye Rift and its Relationship to the South Tibetan Detachment System. *J. Asian Earth Sci.* 29, 722–736. doi:10.1016/j.jseaes.2006.05.003

Zhang, J., SantoshWang, M. X. X., Wang, X., Guo, L., Yang, X., and Zhang, B. (2012). Tectonics of the Northern Himalaya since the India-Asia Collision. *Gondwana Res.* 21, 939–960. doi:10.1016/j.gr.2011.11.004

Zhang, Z., Xiang, H., Dong, X., Ding, H., and He, Z. (2015). Long-lived High-Temperature Granulite-Facies Metamorphism in the Eastern Himalayan Orogen, South Tibet. *Lithos* 212-215, 1–15. doi:10.1016/j.lithos.2014.10.009

Conflict of Interest: The authors declare that the research was conducted in the absence of any commercial or financial relationships that could be construed as a potential conflict of interest.

Publisher's Note: All claims expressed in this article are solely those of the authors and do not necessarily represent those of their affiliated organizations, or those of the publisher, the editors, and the reviewers. Any product that may be evaluated in this article, or claim that may be made by its manufacturer, is not guaranteed or endorsed by the publisher.

Copyright © 2022 Gou, Long, Yan, Shu, Wang, Xu, Zhou and Tian. This is an open-access article distributed under the terms of the Creative Commons Attribution License (CC BY). The use, distribution or reproduction in other forums is permitted, provided the original author(s) and the copyright owner(s) are credited and that the original publication in this journal is cited, in accordance with accepted academic practice. No use, distribution or reproduction is permitted which does not comply with these terms.